

Full Length Article



Super-resolution of clinical CT: Revealing microarchitecture in whole bone clinical CT image data

Lance L. Frazer^{a,*}, Nathan Louis^{a,b}, Wojciech Zbijewski^c, Jay Vaishnav^{d,1}, Kal Clark^e, Daniel P. Nicolella^a

^a Southwest Research Institute, USA

^b University of Michigan, USA

^c John Hopkins University, USA

^d Canon Medical Systems, USA

^e University of Texas Health Science Center at San Antonio, USA

ARTICLE INFO

Keywords:

Super-resolution
Microarchitecture
Fracture risk
Osteoporosis
Clinical CT

ABSTRACT

Osteoporotic fractures, prevalent in the elderly, pose a significant health and economic burden. Current methods for predicting fracture risk, primarily relying on bone mineral density, provide only modest accuracy. If better spatial resolution of trabecular bone in a clinical scan were available, a more complete assessment of fracture risk would be obtained using microarchitectural measures of bone (i.e. trabecular thickness, trabecular spacing, bone volume fraction, etc.). However, increased resolution comes at the cost of increased radiation or can only be applied at small volumes of distal skeletal locations. This study explores super-resolution (SR) technology to enhance clinical CT scans of proximal femurs and better reveal the trabecular microarchitecture of bone. Using a deep-learning-based (i.e. subset of artificial intelligence) SR approach, low-resolution clinical CT images were upscaled to higher resolution and compared to corresponding MicroCT-derived images. SR-derived 2-dimensional microarchitectural measurements, such as degree of anisotropy, bone volume fraction, trabecular spacing, and trabecular thickness were within 16 % error compared to MicroCT data, whereas connectivity density exhibited larger error (as high as 1094 %). SR-derived 3-dimensional microarchitectural metrics exhibited errors <18 %. This work showcases the potential of SR technology to enhance clinical bone imaging and holds promise for improving fracture risk assessments and osteoporosis detection. Further research, including larger datasets and refined techniques, can advance SR's clinical utility, enabling comprehensive microstructural assessment across whole bones, thereby improving fracture risk predictions and patient-specific treatment strategies.

1. Introduction

Osteoporotic fractures commonly occur in the hip and vertebrae and are associated with a \$17 billion burden in healthcare-related costs [1,2]. Not simply an economic burden, osteoporotic fractures are a significant cause of morbidity and mortality in the aging population [3–5]. In fact, hip fractures are fatal in 20 % of cases and permanently disabling in 50 % of cases [6]. It is estimated that 40–46 % of women over 50, and 13–22 % of men over 50 will suffer an osteoporosis-related fracture [7]. With the number of people over 60 projected to nearly triple by 2050 [8], a significant increase in at-risk populations for

fracture is imminent. Thus, the need is immediate to identify those at greatest risk of bone fracture and provide timely intervention.

Over the past two decades, significant progress has been made in our understanding of bone fragility and fracture [9]. However, over the same period, little progress has been made clinically to reliably identify those at risk of fracture. This has been due in part to the narrow breadth of accessible biomarkers that indicate fracture risk. In fact, the only readily agreed upon clinical measure of fracture risk is bone mineral density (BMD). Unfortunately, since BMD only gives a coarse estimate of the amount of mineralized bone per unit volume, BMD alone has only a 30–50 % success rate in predicting fractures [10–12]. Bone is a complex

* Corresponding author.

E-mail address: lance.frazer@swri.org (L.L. Frazer).

¹ Current affiliation: RefleXion Medical.

<https://doi.org/10.1016/j.bone.2024.117115>

Received 20 November 2023; Received in revised form 7 May 2024; Accepted 8 May 2024

Available online 11 May 2024

8756-3282/© 2024 Elsevier Inc. All rights are reserved, including those for text and data mining, AI training, and similar technologies.

structure with an intricate microstructural organization. Characterizing this microstructure (an indicator of bone quality) provides a significantly improved estimate of bone's structural integrity [13–15] compared to BMD. High-resolution peripheral quantitative computed tomography (HR-pQCT) has recently emerged as a promising technology to clinically assess bone microstructure. Unfortunately, HR-pQCT is limited both in its low clinical availability and applicability. Only small volumes of bone at specific peripheral locations can be assessed (i.e., distal tibia, distal radius, etc.). A wealth of information describing bone's structural integrity remains inaccessible, yet whole-bone descriptions of structure are more predictive than single, or few simple measures [16]. A robust solution for assessing bone strength and fracture risk should account for microstructural information like HR-pQCT but should be applicable to full bone volumes at any region of interest (e.g., hip, spine, etc.) like traditional computed tomography (CT).

Super-resolution (SR) technology may offer a solution that stays within the constraints of traditional CT. SR is the process of predicting high-resolution (HR) images from low-resolution (LR) images [17] and is a challenging task in biomedical imaging because of both the difficulty in obtaining quality matched training data [18,19] and the clinical significance of correct/incorrect predictions [20]. However, as artificial intelligence (AI) has rapidly developed, several groups have successfully demonstrated AI-based (more specifically, deep-learning-based, which is a subset of algorithms within AI) SR of medical image data and have provided encouraging results for its application. Notably, Chaudhari et al. used cascaded convolutional neural network SR, DeepResolve, to enhance artificially down-sampled musculoskeletal magnetic resonance imaging (MRI) data (2.1 mm thickness to 0.7 mm thickness) [21,22]. Rudie et al. were also able to enhance MRI data (0.256 × 0.256 mm resolution to 0.256 × 0.128 mm in-plane resolution) using a commercially available U-Net-based convolutional neural network SR product [23]. Li et al. showed that an 8× increase in resolution of inner ear bone could be faithfully recovered using clinical cone beam CT data (0.15 mm isotropic resolution to 0.018 mm isotropic resolution) with a Generative Adversarial network combined with Bayesian inference [24]. Guha et al. successfully performed SR to improve the in-plane spatial resolution from 0.2 mm to 0.15 mm using a special Generative Adversarial Network (GAN-CIRCLE), such that trabecular bone properties (trabecular thickness, trabecular spacing, and trabecular network area density) could be better assessed in ankle scans of healthy volunteers using a multidetector-row CT [25]. While these studies, among others [26–30], have progressed the science of SR in biomedical imaging, there still

remain challenges before traditional clinical CT images of bone can yield microarchitectural detail sufficient for improved fracture risk assessments and osteoporosis detection. First, to be clinically relevant, SR training should be performed on natively obtained LR image data and not down-sampled from HR data to ensure generalizability to actual clinical scanners, since down-sampled data often contains remnants of HR structural information not present in a natively-obtained LR scan (Fig. 1) [21,22,26]. Second, training data should come from a clinical scanner capable of imaging whole bones, such as femurs and vertebrae, and not small-volume, special use-case scanners [24,30]. Finally, quantitative outcome metrics of interest (e.g., trabecular thickness) should be comparable in their accuracy to the quantitative metric to the HR target (i.e., bone microarchitecture). Fracture risk algorithms using microarchitectural measures rely on raw, quantitative values, and thus knowing the actual value is critical.

In this study, we perform 5× SR to proximal femur data obtained from a clinical CT scanner and compare microarchitectural measures to matched MicroCT-derived image data, as well as provide visual comparisons between SR and its HR and LR counterparts. To our knowledge, this work contains the novel contributions of 1) using whole, human long-bone image data, 2) matching image sets from a clinical scanner and a separate, MicroCT scanner, and 3) demonstrating the ability to predict relevant microarchitectural bone metrics LR image data from which microarchitectural measures cannot be obtained.

2. Methods

The overall methods of this work involve creating matched pairs of HR and LR images (taken from different scanners), and training a SR deep learning neural network to predict an HR-like image from LR image input (Fig. 2). The following sections describe these methods in detail.

2.1. Training data

Ten cadaveric femurs from 6 donors (3 male, 3 female, 55–85 years old) were cut 4 in. below the lesser trochanter (isolating the proximal femur) and imaged via two different CT methods. The LR dataset was acquired on a Canon Precision clinical CT operated in an ultra-HR mode (0.4 × 0.5 mm x-ray focal spot, 0.25 mm acquisition slice thickness). Imaging dose (CTDIvol) for the scan was estimated at ~20 mGy. The images were reconstructed using a HR bone kernel (FC30) on a 1024 × 1024 matrix with 0.3125 mm pixel spacing. As such, the discretization

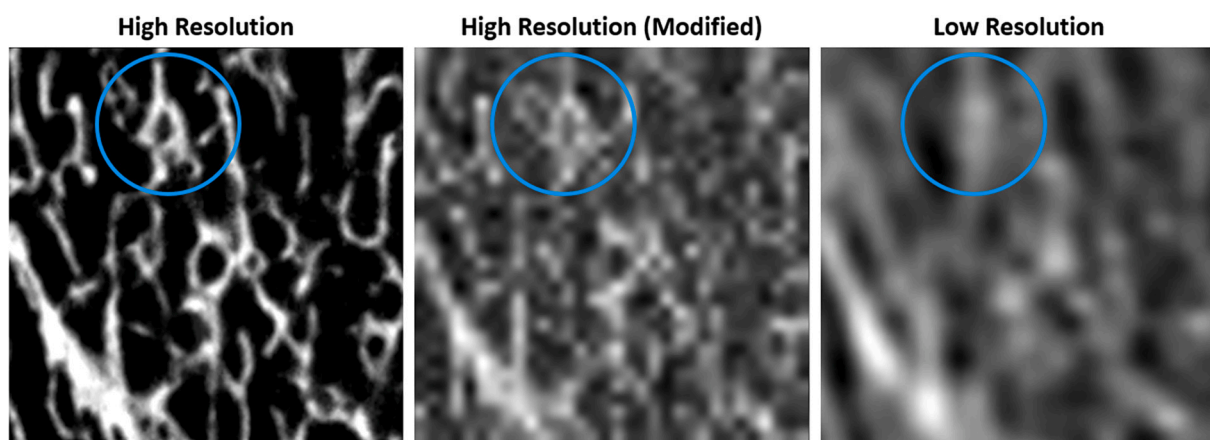


Fig. 1. Comparison between HR data from the femoral head (left), artificially down-sampled HR data (middle), and image data with the same resolution as (middle) but obtained via clinical imaging (right). To create the artificially down-sampled data, we used a 5× down-sampling and added 3 × 3 kernel Gaussian noise. In both the middle and right images, the resolution is 5 times less than the original HR data on the left. Less detail, more blurring, and overall poorer image quality is observed in the clinical scan (right) compared to the down-sampled HR image data (middle). The blue circle highlights specific detail that is still present in the modified HR image that is not present in the native LR image. (For interpretation of the references to colour in this figure legend, the reader is referred to the web version of this article.)

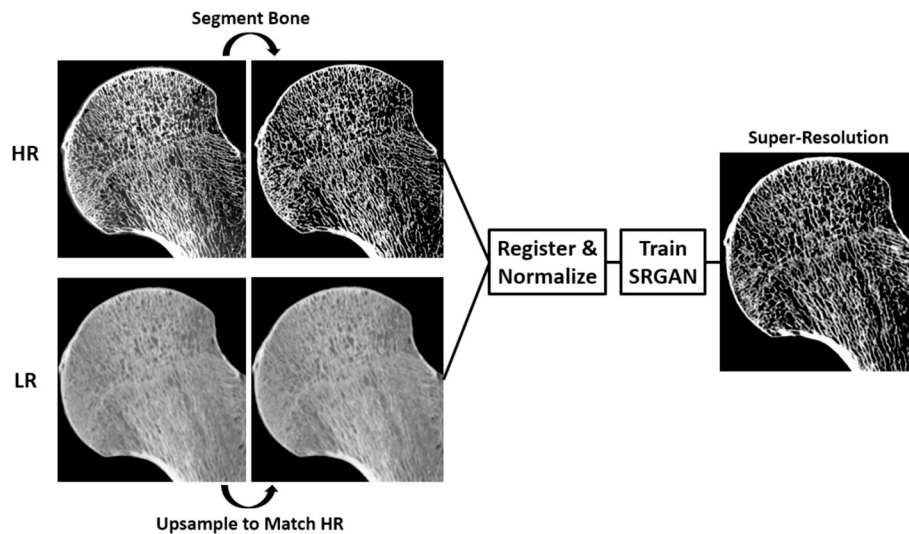


Fig. 2. Overall workflow of creating matched pairs of images to be used as training in the SR deep learning neural network. SRGAN was the network implemented and is described in Section 2.2.

of the LR dataset was 0.3125 mm in the axial plane with 0.25 mm slice thickness. The HR dataset was obtained on a large bore MicroCT (X50-CT, North Star Imaging, Inc.), which is not designed for clinical imaging. The scan was obtained using 100 kV voltage, 80 μ A current, and a focal spot size of 8 μ m with 7920 total projections. Average voxel size (discretization) in the MicroCT image data was isotropic 60 μ m with a range of 56–68 μ m.

For each femur, the LR image data was registered to the HR image data via mutual information [31]. Translation, rotation, and scaling were all allowable in the registration process. Scaling was necessary because of distortions between the two image sets, and the LR image data often needed 1–2 % scaling in at least one axis to ensure the best possible alignment (automatically applied via mutual information). The LR data was upsampled using cubic interpolation to the same voxel spacing as the MicroCT (0.3125 \times 0.3125 \times 0.25 mm \rightarrow \sim 0.6 mm isotropic resolution), resulting in image-to-image correspondence. To avoid overfitting unimportant (non-bone) data and noise within each MicroCT scan, bone in the MicroCT images was automatically segmented via U-Net deep learning, and the resulting segmentation was inverted and used to set the underlying grayscale values to zero. For each bone, a separate U-Net model was trained on a few slices of manual segmentations and applied to the rest of the slices in the scan. Each 5-layer U-NET model was trained and implemented in Dragonfly using their built-in segmentation wizard, which uses TensorFlow deep learning packages. A patch size of 64 was used with a stride ratio of 0.25. A CategoricalCrossentropy [32] loss function was implemented with the Adadelata optimization algorithm [33] using a decay of 0, an epsilon of 1e-7, a learning rate of 1, and a rho value of 0.95. The image data was augmented 10 times using a combination of flips (horizontal and vertical), rotations (up to 180 degrees), shear (up to 2 degrees), scale (90–110 %), and brightness (80–120 %). Images from the matched femurs were exported for training in all 3 planes (frontal, axial, and sagittal). Each femur provided \sim 4 k images between all 3 planes, and thus the full training data consisted of \sim 40 k full images (Fig. 3). We split this data into a training and validation set using an 80/20 ratio. Hence, we train our SR model on 32 k images and validate our model parameters on the remaining 8 k images. All image data were processed using Dragonfly v2022.2 (Comet Technologies, Montreal, Quebec).

2.2. Super-resolution

To perform deep-learning based SR, we used a Super Resolution Generative Adversarial Network (SRGAN) [34] to produce SR images

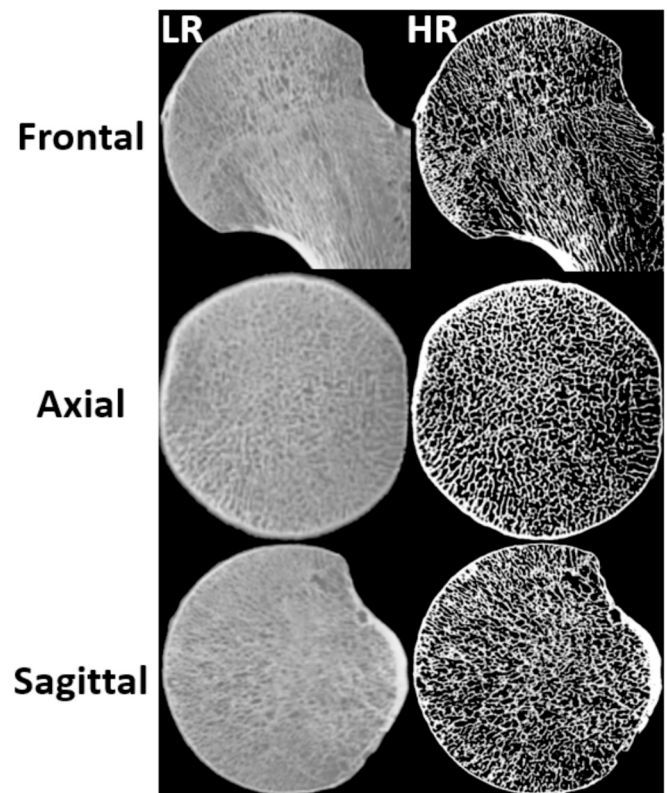


Fig. 3. Example training pairs taken from the femoral head. LR image data is on the left column, and the segmented MicroCT image data is on the right. Here, the femoral head is zoomed in on to show the differences between the LR and HR image data.

from LR image inputs. The model was adopted from an open-source third party repo (<https://github.com/leftthomas/SRGAN>) and implemented outside of Dragonfly. The SRGAN model uses adversarial training [35] to generate SR images that exist in the same image distribution as HR images. The SR generator model is a 5-block deep residual network [36] used to generate an output image with 4 \times scaling of the input image. Note that the original resolution of the LR image is 5 \times less than the HR, but the network was implemented with a 4 \times scaling.

Effectively, the LR data was sampled to be 4× less than the HR image resolution after the LR images were upsampled for image alignment. The discriminator was a convolutional network with a sigmoid function to predict whether the input is an HR or LR image. For a detailed description of SRGAN, see [34]. We trained both the generator and discriminator from scratch for 10 epochs with a batch size of 4, using a learning rate of 1e-4 for the generator and 1e-8 for the discriminator. To train, a random crop of 400 × 400 was taken from the HR image, and the corresponding region in the LR image is down-sampled by 4× to 100 × 100. This pair represented the LR input and the HR target image. Due to scan-to-scan variation, the dynamic range of pixel values between bone scans may differ significantly. Data were normalized for each bone by setting the zero grayscale values to the next lowest grayscale value because some scans had the second lowest value at 1, while others had values as high as 150. In both cases, these second lowest values were marrow space and not bone. Subsequently, the grayscale values were normalized to 0–255 and converted to 8-bit PNG images. In preliminary testing, we observed significant (qualitative) image degradation past 10 epochs. Images appeared blurry with poor distinction between individual trabeculae.

The discriminator was trained with a simple classification loss, while the generator used a multi-part loss including the perceptual loss [37,38]. The perceptual loss was measured between the feature maps of a Visual Geometry Group (VGG, pretrained on ImageNet) network output from both the HR and SR images. This encourages the SR image to be perceptually similar to the HR image rather than strictly enforcing pixel-wise agreement which tends to produce overly smooth outputs [34,38,39]. The total generator loss was a summation of the mean-squared error between the SR and HR images, mean-squared error on the VGG feature maps (perceptual loss), the adversarial classification loss, and a total-variation loss [40] (Eq. (1)). The SRGAN model was developed and implemented in PyTorch [34] on an Nvidia GeForce RTX 2080 Ti GPU. Training for 10 epochs took ~12 h.

$$L_G = \lambda_{MSE}L_{MSE} + \lambda_{per}L_{per} + \lambda_{adv}L_{adv}^G + \lambda_{tv}L_{tv} \quad (1)$$

2.3. Test set

Two cadaveric femurs from 2 donors (left femur from a 63-year-old male and a right femur from a 71-year-old female) were used as a test set and were not included in the training or validation set. These bones were imaged and processed in the same manner as during training.

2.4. Analysis

For GANs, the network performances are generally measured using peak signal-to-noise ratio (PSNR) and structural similarity (SSIM) [41]. PSNR measures absolute error between the reference and target image, while SSIM is a perceptual metric that measures image quality degradation between two images through structural changes. PSNR is defined in Eq. (2) using the squared maximum image pixel value (MAX_I^2) and the mean-squared error (MSE) between the SR and HR images.

$$PSNR = 10^* \log_{10} \left(\frac{MAX_I^2}{MSE} \right) \quad (2)$$

SSIM is shown in Eq. (3), comparing the luminance, contrast, and structure between two images using the computed mean μ and standard deviation σ pixel values of each image.

$$SSIM(\mathbf{x}, \mathbf{y}) = \frac{(2\mu_x\mu_y + C_1)(2\sigma_{xy} + C_2)}{(\mu_x^2 + \mu_y^2 + C_1)(\sigma_x^2 + \sigma_y^2 + C_2)} \quad (3)$$

$C_1 = 0.01^2$ and $C_2 = 0.03^2$ provide numerical stability in the case that μ and σ values are near zero.

In practice, SSIM is not computed over the entire image but rather

local windows to account for spatial variations in quality. The reported SSIM is the average across all local windows in the image.

PSNR has been shown to not reliably capture perceived visual quality [41]. This effect is likely exacerbated in the present study because of the abundance of zero-pixels in the bone scans. We therefore elected to use SSIM to select the best performing model from the validation set. For each test bone, SR images were produced in each of the three anatomical planes. Results were similar in all three planes and between each test bone, and therefore, only one test bone (male) in the frontal plane is reported. However, visual comparisons for the female test bone are provided (frontal plane). Also, using frontal plane images, an axial view is provided to show the error that is introduced by stacking two-dimensional (2D) slices. SR-generated images from the frontal plane, when stacked and viewed axially, highlight a weakness in our SR approach.

Since the SRGAN works 2D image planes, 2D microstructural measurements were first obtained in a small set of representative trabecular regions of interest to illustrate performance in the native domain of the SR network. The 2D microarchitectural measures were taken from three 10x10mm crops, one at the femoral head, one at the femoral neck, and one in the greater trochanter. Considering that future clinical applications of the trabecular metrics are likely to involve three-dimensional (3D) analyses, we have further quantified the accuracy of 3D measurements using 24 spatially dispersed, 10x10x10mm cubes of image data throughout the entire proximal femur (Fig. 4, left).

To calculate the 2D microarchitectural parameters (degree of anisotropy (DA), trabecular thickness (Tb.Th.), trabecular separation (Tb.Sp.), bone volume fraction (BV/TV), and connectivity density (Conn.D)), the SR images were segmented via Adaptive Gaussian segmentation [42] and processed using Dragonfly's Bone Analysis package. For the Adaptive Gaussian segmentation, the sigma parameter (amount of variation or dispersion of the set of values within the defined neighborhood) was set to 15, and the offset (constant subtracted from the weighted sum of neighborhood to calculate the local threshold value) was set to 0. These values were selected based on prior experience with segmenting HR image data. The segmentation was performed with a sliding 3x3mm square kernel.

3D microarchitectural parameters (eigenvector 1 and 3 of the fabric tensor and their associated eigenvalues (using mean intercept length), Tb.Th., Tb.Sp., and BV/TV) were calculated using medtool 4.6 (Dr. Pahr Ingenieure e.U, Pfaffstätten, Austria). For the 3D analyses, frontal images were used, and the 3D segmentation was a product of stacking 2D segmentations of each slice.

For all metrics, errors were calculated as:

$$\frac{\text{Ground Truth (HR)} - \text{Predicted Value (SR)}}{\text{Ground Truth (HR)}}$$

where a positive error is an underprediction, and a negative error is an overprediction.

3. Results

3.1. Super-resolution deep learning network performance

We selected the best performing model from the epoch that produces the highest SSIM on the validation set using randomly selected image patches. This is an SSIM of 0.6111 across the image patches. We use this trained model for evaluation on the unseen test set.

We report the corresponding PSNR and SSIM on validation set on the entire image as 19.333 dB and 0.7917, respectively.

On the test set, for the unseen bones, these values are 18.437 dB and 0.7725 (63-year-old male) and 16.671 dB and 0.7589 (71-year-old female). During training and validation, image patches are randomly sampled from each image to be evaluated. While on the test set, we evaluate the entire image. Hence, the sampling of a single image patch

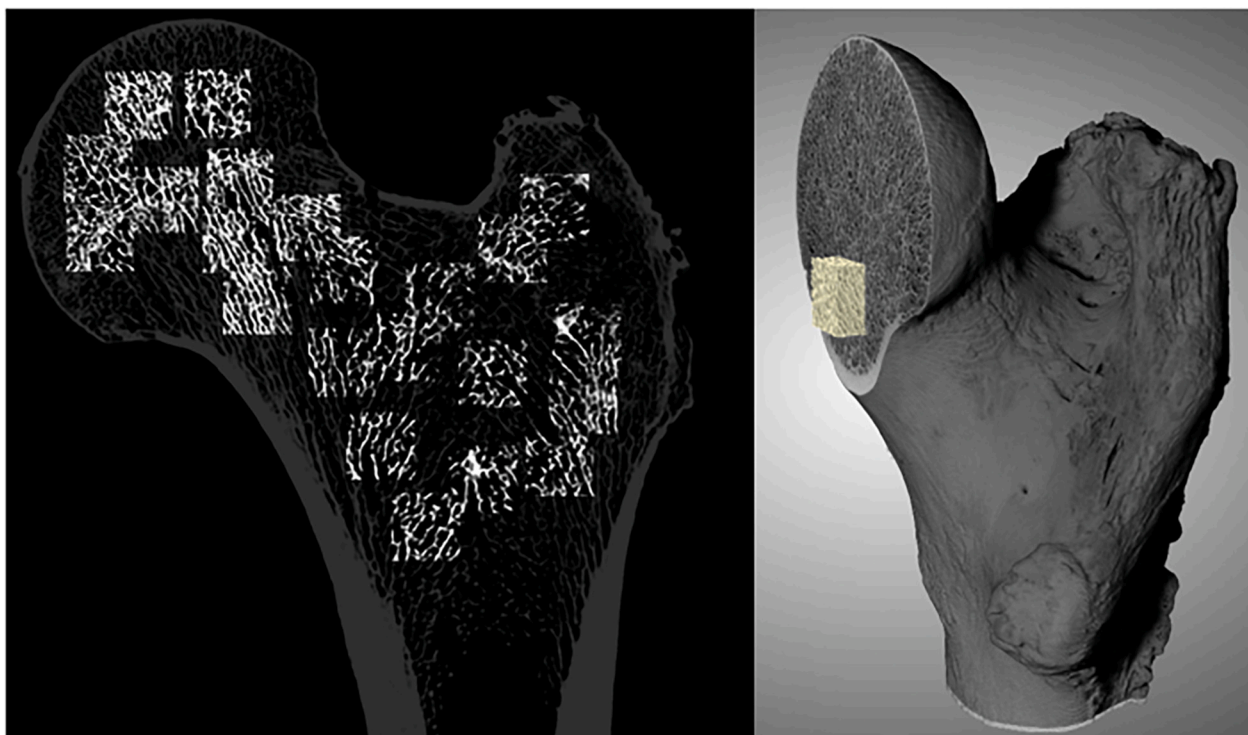


Fig. 4. Left: selected regions to assess 3D microarchitecture. Right: example 3D image data (beige) taken from one of the regions shown on the left using a sagittal cutting plane. (For interpretation of the references to colour in this figure legend, the reader is referred to the web version of this article.)

may result in a lower score for the validation set because of the abundance of black regions in the CT scans.

3.2. Bone analysis

SR images from the frontal plane appear perceptually similar to the MicroCT image data for the femoral head (Fig. 5), femoral neck (Fig. 6), and greater trochanter (Fig. 7) of the male test bone; the female test bone showed similar qualitative results (Fig. 8). 2D microarchitectural measures from the SR image data such as DA, BV/TV, and Tb.Th. show good agreement with the MicroCT image data (maximum error of 12 % with

average error below 5 %) for the femoral head (Table 1), femoral neck (Table 2), and the superior portion of the greater trochanter (Table 3). Conn.D measures show poor agreement between the two image sets. Tb.Th. was consistently overpredicted in the SR image data with minor error in the diaphyseal region and femoral neck, while the femoral head and greater trochanter had the largest error.

Overall, 3D microarchitectural measures taken from the femoral head show worse agreement with the MicroCT image data than the 2D analysis. Tb.Th. and the two eigenvalues show the best agreement (average error of 7 % and 5–7 %, respectively), while BV/TV and eigenvectors show the poorest agreement (12 % and 18–19 degrees,

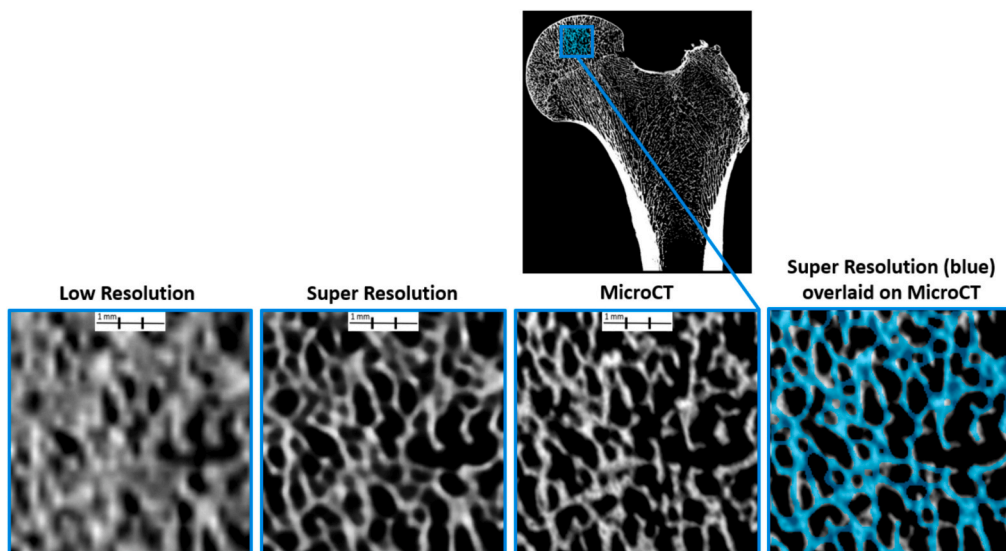


Fig. 5. Comparisons between LR, SR, and MicroCT image data taken from a frontal section in the femoral head for the 63-year-old male. On the right, the segmented SR image data are overlaid on the MicroCT image data. Microarchitectural parameters from the section are shown in the upper left. The PSNR and SSIM of the LR slice was 12.27 dB and 0.14, respectively. The PSNR and SSIM of the SR data was 13.46 dB and 0.47, respectively. Scale bar shows 1 mm increments.

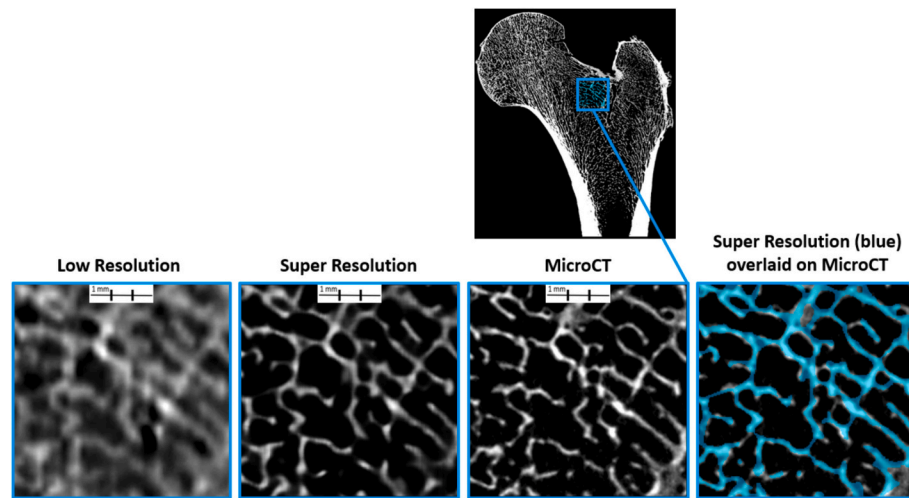


Fig. 6. Comparisons between LR, SR, and MicroCT image data taken from a frontal section in the femoral neck for the 63-year-old male. On the right, the segmented SR image data are overlaid on the MicroCT image data. Microarchitectural parameters from the section are shown in the upper left. The PSNR and SSIM of the LR slice was 12.35 dB and 0.14, respectively. The PSNR and SSIM of the SR data was 13.23 dB and 0.48, respectively. Scale bar shows 1 mm increments.

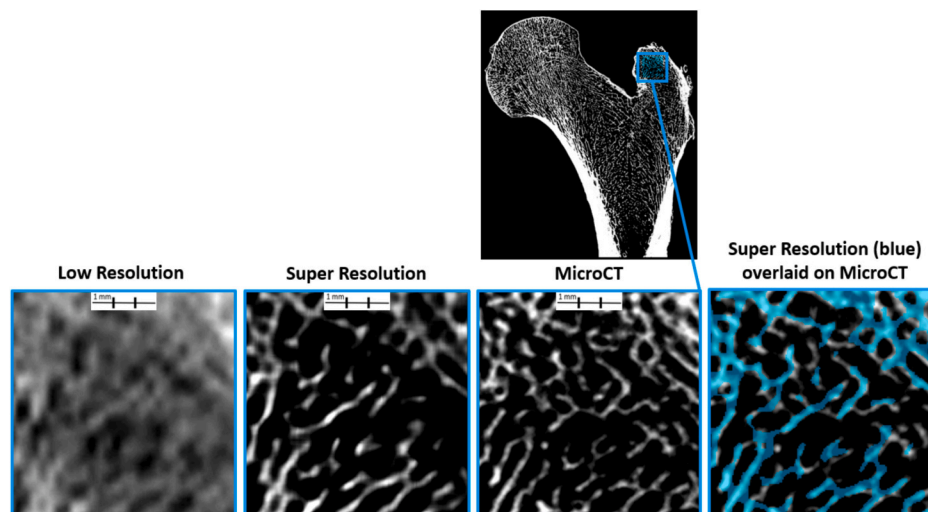


Fig. 7. Comparisons between LR, SR, and MicroCT image data taken from a frontal section in the greater trochanter for the 63-year-old male. On the right, the segmented SR image data are overlaid on the MicroCT image data. Microarchitectural parameters from the section are shown in the upper left. The PSNR and SSIM of the LR slice was 12.48 dB and 0.15, respectively. The PSNR and SSIM of the SR data was 13.44 dB and 0.48, respectively. Scale bar shows 1 mm increments.

respectively) (Table 4). Tb.Sp. yielded moderate agreement (9 % error). Out-of-plane images from the SR image data appear to be of poorer quality when compared to the natively processed image plane (Fig. 9). It should be noted that the application of the same segmentation algorithm on the native LR images yielded a substantial over-estimation of bone that resulted in unusable trabecular measurements.

4. Discussion

In this study, we applied SR to relatively coarsely sampled ($0.3125 \times 0.3125 \times 0.250$ mm) proximal femur CT image data and predicted ~ 0.06 mm isotropic image data with reduced noise and sharp contrast between bone and non-bone. To our knowledge, this is the first implementation of $>4\times$ SR to recover microarchitectural parameters using a clinical scanner capable of whole bone in vivo imaging. The SR-derived microarchitectural measures show good agreement to MicroCT-derived microarchitectural measures and is especially significant because microarchitectural parameters were not recoverable from the native LR image data using the same segmentation algorithms as applied to the SR

images. Microarchitectural measures have been associated with improved fracture risk prediction [43–48].

Overall, 2D microarchitectural measures from the SR image data were in good agreement with the microCT-derived measures. Tb.Th., BV/TV, and principal directions from the fabric tensor were within ~ 10 % of the MicroCT-derived measures. Tb.Sp. was predicted well in some areas (femoral neck) and poorer in other areas (femoral head) with errors between 2 and 16 %. Conn.D showed the poorest comparison and highlights a weakness in 2D SR. Small instances of bone that likely go in- and out-of-plane are not correctly predicted in 2D. The SR network may interpret this as noise (or there is nothing there to pick up from the LR image data), and thus the bone is not recovered in the SR image data. As such, these small instances of bone in the 2D MicroCT image data create incongruity in the bone microarchitecture, which lowers the connectivity density. The SR data emphasized in-plane connections, and overestimates the overall connectivity without the small, seemingly unconnected instances of bone. This weakness is also shown in the 3D microarchitectural predictions. While Conn.D is not calculated by medtool software, we observe an over-estimation in trabecular spacing.

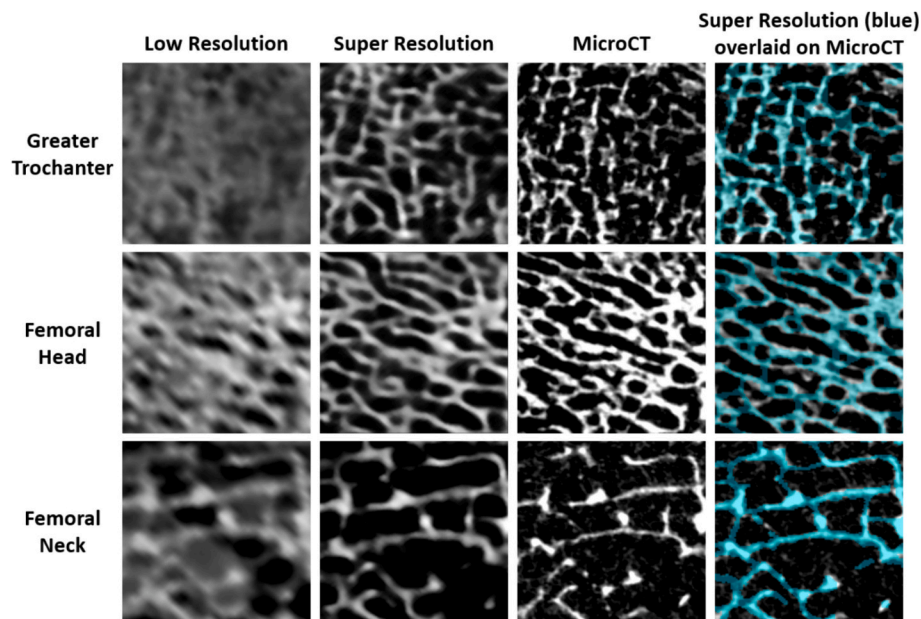


Fig. 8. Comparisons between LR, SR, and MicroCT image data taken from frontal section taken from the greater trochanter, femoral head, and femoral neck for the 71-year-old female. On the right, the segmented SR image data are overlaid on the MicroCT image data. For the LR data, PSNR values were 10.7178, 6.7198, and 9.2041 for the greater trochanter, femoral head, and femoral neck, respectively. SSIM values were 0.0117, 0.0146, and 0.0199. For the SR data, PSNR values were 8.3807, 7.6733, and 9.1579 for the greater trochanter, femoral head, and femoral neck, respectively. SSIM values were 0.0773, 0.0321, and 0.2439.

Table 1

2D microarchitectural parameters measured at the femoral head for the 63-year-old male. Error of the SR compared to the MicroCT data is shown parenthetically.

Bone metric	Super resolution	MicroCT ground truth
DA	0.99 (0 %)	0.99
BV/TV	40 % (5 %)	42 %
Tb.Th. (mm)	0.46 (−7 %)	0.43
Tb.Sp. (mm)	0.73 (−16 %)	0.63
Conn.D (mm ^{−2})	35.26 (−31 %)	26.93

Table 2

2D microarchitectural parameters measured at the femoral neck for the 63-year-old male. Error of the SR compared to the MicroCT data is shown parenthetically.

Bone metric	Super resolution	MicroCT ground truth
DA	1 (0 %)	1
BV/TV	23 % (8 %)	25 %
Tb.Th. (mm)	0.37 (12 %)	0.42
Tb.Sp. (mm)	1.29 (−2 %)	1.26
Conn.D (mm ^{−2})	10.97 (2 %)	11.14

Table 3

2D microarchitectural parameters measured at the superior portion of the greater trochanter for the 63-year-old male. Error of the SR compared to the MicroCT data is shown parenthetically.

Bone metric	Super resolution	MicroCT ground truth
DA	1 (1 %)	0.99
BV/TV	31 % (−3 %)	30 %
Tb.Th. (mm)	0.39 (−11 %)	0.35
Tb.Sp. (mm)	0.85 (−15 %)	0.74
Conn.D (mm ^{−2})	24.18 (−120 %)	10.97

The overestimation in 3D is likely a function of the same issue. Since in- and out-of-plane bone is not correctly captured, larger gaps are observed between the trabeculae and finer detail is lost. The issue of larger gaps is

Table 4

Microarchitectural parameter errors from the 3D cubes of SR image data compared to HR for the 63-year-old male. In this data, the Z vector is through the thickness of the slices (perpendicular to the frontal plane). The X vector runs medial to lateral, and the Y vector runs inferior to superior. The standard deviation measures (Tb.Th. (std) and Tb.Sp. (std)) are standard deviations within the same image cube of data (intra-variability). The ± after the error are standard deviation measures between the 3D cubes of data (inter-variability).

	Error
Tb.Th. (mean)	−7 % ± 7 %
Tb.Th. (std)	18 % ± 12 %
Tb.Sp. (mean)	9 % ± 5 %
Tb.Sp. (std)	9 % ± 8 %
BV/TV	−12 % ± 7 %
Eigenvector 1 Angle (degrees)	18 ± 6
Eigenvalue 1	5 % ± 4 %
Eigenvector 3 Angle (degrees)	19 ± 6
Eigenvalue 3	7 % ± 5 %

especially evident in Fig. 9. SR images predicted from frontal plane LR images show poor visual comparisons to the MicroCT data when looking at the axial plane. However, SR images from axial plane LR input correctly shows finer detail observable in the MicroCT data. While averaging data from each of the three planes may improve the results, we believe that the resulting images may induce extra blurring with any misalignment in the images and would also introduce error from each of the three planes. We therefore did not pursue this approach. Nonetheless, since all three image planes would be available, in a clinical application, it may be prudent to independently use all three imaging planes to assess a given bone to get a more complete presentation of the bone. The 3D results also show greater error in BV/TV than what is observed in 2D. Since the 3D volumes are built from stacking 2D images and segmentations, the small 2D errors compound through the thickness.

In general, the network performed equally well in various 2D locations in the proximal femur with a bit of performance degradation (over-predicting both Tb.Th. and Tb.Sp.) in the greater trochanter (seen in

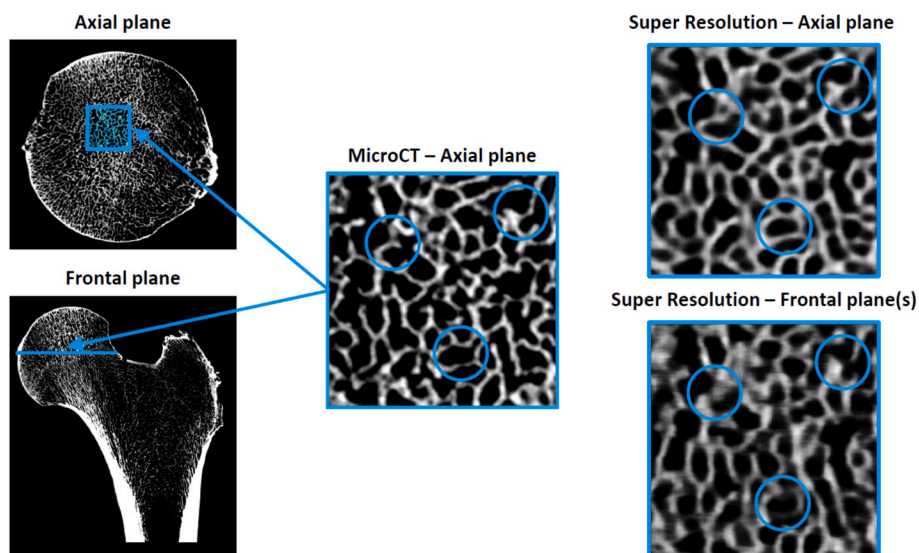


Fig. 9. Comparisons between SR processed from both axial (top) and frontal (bottom) planes and MicroCT image data taken from an axial section in the femoral head (middle) for the 71-year-old female. The blue circled regions highlight the accurate reconstructions from the axial plane as compared to the reconstructed frontal planes. (For interpretation of the references to colour in this figure legend, the reader is referred to the web version of this article.)

Figs. 7 and 8). This is likely a consequence of too little training data and thinner, more sparse bone in that particular part of the femur. Since the greater trochanter makes up a relatively smaller part of the bone, more training data is likely needed to better represent the type of microarchitecture most often observed in this location. Moreover, the trabecular bone in the greater trochanter appears thinner and sparser than bone in the other observed locations (e.g. femoral head), and the LR data does not capture this detail well enough to accurately reconstruct the microarchitecture. Nonetheless, the microarchitectural parameters (in 2D) from this region were still reasonably predicted, although a 3D prediction in this location may not compare well to MicroCT data. The greater trochanter may also be less consequential when assessing fracture risk and femoral strength compared to the femoral head/neck. Performance degradation in this location may therefore be acceptable. However, it should be noted that further work must be performed with osteoporotic bone to test if the problem is specific to thin and sparse bone, or if it's a problem of insufficient training data. Given the overall sparseness and thin microarchitecture of the female test bone (which was predicted well in Fig. 9), we believe the problem is better attributed to insufficient training samples of the greater trochanter and the unique microarchitecture in this specific area, though future work should test this.

The SSIM and PSNR evaluation metrics are poorer than other comparative studies that report these metrics ([21] reports 0.7 and 26 dB for the SSIM and PSNR, respectively, compared to our values of 0.76 and 17 dB, and [26] reports 0.94 and 29.4 dB for the SSIM and PSNR, respectively). Because the image data came from two different scanners, and the SR data was created from a SR model trained with segmented HR data (which was not used for the calculation of PSNR and SSIM), it is difficult to achieve a high SSIM value (>0.8). However, the intent of this study was to focus on the trabecular microarchitecture and the accurate recovery of metrics relevant to fracture risk. Thus, little effort was given to improving these metrics, as we deemed the study successful when it became possible to reliably segment the SR data and compare it to the HR data.

Successful SR of clinical CT image data has significant implications for clinical fracture risk assessment. In *ex vivo* studies, microarchitectural information across whole-bone image data has enabled highly accurate patient-specific finite element models, which supports the importance of microarchitecture in bone strength, and therefore, fracture risk [13–15,49]. Moreover, after performing a large

retrospective meta-analysis on the use of microarchitectural measures in fracture risk, the Bone Microarchitecture International Consortium (BoMIC) concluded that microarchitectural measures are significant predictors of fracture risk and are encouraging their use in future algorithm development [50]. In each of the studies that the BoMIC assessed, HR-pQCT was the prescribed imaging modality, which only provided small volumes of bone to scrutinize at peripheral skeletal locations away from the site of fracture (e.g. distal tibia). Clinical accessibility to microarchitectural information at whole-bone scales for any bone of interest may create new paradigms for fracture risk assessments.

This study has several limitations. The training and validation set were small. While the training and validation set included ~ 40 k images that are further cropped into smaller images to create 250 k+ training samples, the images came from only 6 donors. The donors were older individuals, and it is unknown how well the network would perform with younger individuals with more robust microarchitecture. Similarly, the test set only contained two femurs. However, since the network is predicting HR data across the entire bone, we find it encouraging that different areas with different microarchitectures are predicted well.

Another clinically limiting weakness of the current study is the clinical CT scanner, which is not representative of commonly available CT devices. The Aquilion Precision employs state-of-the-art hardware to achieve $1.5\times - 2\times$ improved spatial resolution compared to current conventional CT systems, enabling visualization of down to ~ 150 μm details in appropriately optimized scan protocols [51–54]. Earlier studies have found appreciably better correlations against uCT of trabecular measurements obtained on Precision CT operated in an ultra-high resolution mode (the same as used in the current study, 0.25 mm slice thickness) compared to standard resolution imaging (0.5 mm slice thickness) - for example, Tb.Sp. correlation coefficient of 0.74 at ultra-high resolution vs. <0.1 at standard resolution [55]. An algorithm that works with other, more ubiquitous scanners would provide proportionality more clinical benefit. However, it is worth noting that photon-counting CT, first commercialized in the US in 2021 and widely anticipated to become a clinical standard in the future, may provide spatial resolution comparable to or slight higher than that of the Aquilion Precision CT [56–59] and may thus similarly benefit from the proposed SR technique.

Since the acceptable alignment of the LR image data with the MicroCT image data required scaling of 1–2 % of the LR image data, the resulting SR images may over- or under-estimate the volume of bone by

a similar amount. We find this to be an acceptable tradeoff, as the image alignment using real image data from two different scanners ensures that the network is generalizable to an actual clinical scanner for whole bones and does not include detail in the LR image data that would not normally be present (Fig. 1). Finally, the SR results do not enable the calculation of mineralization since the contrast is relative to the normalization scheme used in the training. The SR image data tends to be more binary in its presentation, and any visual contrast should not necessarily be interpreted as differences in mineralization.

5. Conclusion

In conclusion, SR was implemented for whole, proximal femurs and demonstrates the applicability of such technology for clinical radiology. In general, we found that deriving microarchitectural parameters on a slice-by-slice basis (2-dimensional) yielded better results than 3-dimensional measures. We attribute this to the 2-dimensional nature of the deep learning SR model. We also found that areas with sparser bone (e.g., the greater trochanter) was poorly predicted from the SR model compared to areas of bone that had a higher bone volume fraction (e.g., the femoral head). This work helps to better reveal bone microarchitecture at whole-bone scales, which may help improve bone fracture predictions.

Funding

This work was supported by Canon Medical Systems USA, Inc., San Antonio Medical Foundation, and by the National Institutes of Health [grant number R01-EB-029446].

CRedit authorship contribution statement

Lance L. Frazer: Writing – review & editing, Writing – original draft, Methodology, Funding acquisition, Formal analysis, Data curation, Conceptualization. **Nathan Louis:** Writing – original draft, Methodology, Formal analysis. **Wojciech Zbijewski:** Writing – review & editing, Writing – original draft, Resources, Methodology, Data curation. **Jay Vaishnav:** Writing – review & editing, Resources, Project administration, Funding acquisition. **Kal Clark:** Writing – review & editing, Supervision, Methodology. **Daniel P. Nicoletta:** Writing – review & editing, Supervision, Resources, Funding acquisition, Conceptualization.

Declaration of competing interest

The authors declare the following financial interests/personal relationships which may be considered as potential competing interests: Lance Frazer reports financial support was provided by Canon Medical Systems USA Inc. Jay Vaishnav reports a relationship with Canon Medical Systems USA Inc. that includes: employment. If there are other authors, they declare that they have no known competing financial interests or personal relationships that could have appeared to influence the work reported in this paper.

Data availability

The data that has been used is confidential.

References

- [1] S. Ferrari, J.Y. Reginster, M.L. Brandi, J.A. Kanis, J.P. Devogelaer, J.M. Kaufman, J. M. Feron, A. Kurth, R. Rizzoli, Unmet needs and current and future approaches for osteoporotic patients at high risk of hip fracture, *Arch. Osteoporos.* 11 (1) (2016) 37.
- [2] R. Burge, B. Dawson-Hughes, D.H. Solomon, J.B. Wong, A. King, A. Tosteson, Incidence and economic burden of osteoporosis-related fractures in the United States, 2005–2025, *J. Bone Miner. Res.* 22 (3) (2007) 465–475.
- [3] L.J. Melton 3rd, Adverse outcomes of osteoporotic fractures in the general population, *J. Bone Miner. Res.* 18 (6) (2003) 1139–1141.
- [4] J.A. Kanis, A. Oden, O. Johnell, C. De Laet, B. Jonsson, A.K. Oglesby, The components of excess mortality after hip fracture, *Bone* 32 (5) (2003) 468–473.
- [5] O. Johnell, J.A. Kanis, A. Oden, I. Sernbo, I. Redlund-Johnell, C. Pettersson, C. De Laet, B. Jonsson, Mortality after osteoporotic fractures, *Osteoporos. Int.* 15 (1) (2004) 38–42.
- [6] National Clinical Guideline, C, National Institute for health and clinical excellence: guidance, in: *Osteoporosis: Fragility Fracture Risk: Osteoporosis: Assessing the Risk of Fragility Fracture*, Royal College of Physicians (UK) National Clinical Guideline Centre., London, 2012.
- [7] J.A. Kanis, O. Johnell, A. Oden, I. Sembo, I. Redlund-Johnell, A. Dawson, C. De Laet, B. Jonsson, Long-term risk of osteoporotic fracture in Malmö, *Osteoporos. Int.* 11 (8) (2000) 669–674.
- [8] United Nations, World Population Prospects: The 2008 Revision, Population Division of the Department of Economic and Social Affairs of the United Nations Secretariat, 2009.
- [9] C.J. Hernandez, M.C. van der Meulen, Understanding bone strength is not enough, *J. Bone Miner. Res.* 32 (6) (2017) 1157–1162.
- [10] B.R. McCreadie, S.A. Goldstein, Biomechanics of fracture: is bone mineral density sufficient to assess risk? *J. Bone Miner. Res.* 15 (12) (2000) 2305–2308.
- [11] J. Homminga, B.R. McCreadie, T.E. Ciarelli, H. Weinans, S.A. Goldstein, R. Huiskes, Cancellous bone mechanical properties from normals and patients with hip fractures differ on the structure level, not on the bone hard tissue level, *Bone* 30 (5) (2002) 759–764.
- [12] J.A. Kanis, O. Johnell, A. Oden, A. Dawson, C. De Laet, B. Jonsson, Ten year probabilities of osteoporotic fractures according to BMD and diagnostic thresholds, *Osteoporos. Int.* 12 (12) (2001) 989–995.
- [13] T. Gross, D.H. Pahr, P.K. Zysset, Morphology-elasticity relationships using decreasing fabric information of human trabecular bone from three major anatomical locations, *Biomech. Model. Mechanobiol.* 12 (4) (2013) 793–800.
- [14] G. Maquer, S.N. Musy, J. Wandel, T. Gross, P.K. Zysset, Bone volume fraction and fabric anisotropy are better determinants of trabecular bone stiffness than other morphological variables, *J. Bone Miner. Res.* 30 (6) (2015) 1000–1008.
- [15] D.H. Pahr, P.K. Zysset, A comparison of enhanced continuum FE with micro FE models of human vertebral bodies, *J. Biomech.* 42 (4) (2009) 455–462.
- [16] T.L. Bredbenner, R.L. Mason, L.M. Havill, E.S. Orwoll, D.P. Nicoletta, Osteoporotic Fractures in Men, S, Fracture risk predictions based on statistical shape and density modeling of the proximal femur, *J. Bone Miner. Res.* 29 (9) (2014) 2090–2100.
- [17] P. Purkait, B. Chanda, Super resolution image reconstruction through Bregman iteration using morphologic regularization, *IEEE Trans. Image Process.* 21 (9) (2012) 4029–4039.
- [18] J.-Y. Zhu, T. Park, P. Isola, A.A. Efros, Unpaired image-to-image translation using cycle-consistent adversarial networks, in: *Proceedings of the IEEE International Conference on Computer Vision, 2017*, pp. 2223–2232.
- [19] Z. Zhang, S. Yu, W. Qin, X. Liang, Y. Xie, G. Cao, Self-supervised CT super-resolution with hybrid model, *Comput. Biol. Med.* 138 (2021) 104775.
- [20] O. Oren, B.J. Gersh, D.L. Bhatt, Artificial intelligence in medical imaging: switching from radiographic pathological data to clinically meaningful endpoints, *Lancet Digit. Health* 2 (9) (2020) e486–e488.
- [21] A.S. Chaudhari, Z. Fang, F. Kogan, J. Wood, K.J. Stevens, E.K. Gibbons, J.H. Lee, G. E. Gold, B.A. Hargreaves, Super-resolution musculoskeletal MRI using deep learning, *Magn. Reson. Med.* 80 (5) (2018) 2139–2154.
- [22] A.S. Chaudhari, K.J. Stevens, J.P. Wood, A.K. Chakraborty, E.K. Gibbons, Z. Fang, A.D. Desai, J.H. Lee, G.E. Gold, B.A. Hargreaves, Utility of deep learning super-resolution in the context of osteoarthritis MRI biomarkers, *J. Magn. Reson. Imaging* 51 (3) (2020) 768–779.
- [23] J.D. Rudie, T. Gleason, M.J. Barkovich, D.M. Wilson, A. Shankaranarayanan, T. Zhang, L. Wang, E. Gong, G. Zaharchuk, J.E. Villanueva-Meyer, Clinical assessment of deep learning-based super-resolution for 3D volumetric brain MRI, *Radiol. Artif. Intell.* 4 (2) (2022) e210059.
- [24] H. Li, R.G.N. Prasad, A. Sekuboyina, C. Niu, S. Bai, W. Hemmert, B. Menze, Micro-CT synthesis and inner ear super resolution via generative adversarial networks and Bayesian inference, in: *2021 IEEE 18th International Symposium on Biomedical Imaging (ISBI)*, 2021, pp. 1500–1504.
- [25] I. Guha, S.A. Nadeem, C. You, X. Zhang, S.M. Levy, G. Wang, J.C. Torner, P. K. Saha, Deep learning based high-resolution reconstruction of trabecular bone microstructures from low-resolution CT scans using GAN-CIRCLE, in: *Proc SPIE Int Soc Opt Eng*, 2020, p. 11317.
- [26] X. Xie, Y. Wang, S. Li, L. Lei, Y. Hu, J. Zhang, Super-resolution reconstruction of bone micro-structure micro-CT image based on auto-encoder structure ^{*}, in: *2019 IEEE International Conference on Robotics and Biomimetics (ROBIO)*, 2019, pp. 1568–1575.
- [27] H. Xie, T. Zhang, W. Song, S. Wang, H. Zhu, R. Zhang, W. Zhang, Y. Yu, Y. Zhao, Super-resolution of pneumocystis carinii pneumonia CT via self-attention GAN, *Comput. Methods Programs Biomed.* 212 (2021) 106467.
- [28] Z. Song, X. Zhao, Y. Hui, H. Jiang, Progressive back-projection network for COVID-CT super-resolution, *Comput. Methods Programs Biomed.* 208 (2021) 106193.
- [29] B. Huang, H. Xiao, W. Liu, Y. Zhang, H. Wu, W. Wang, Y. Yang, Y. Yang, G. W. Miller, T. Li, MRI super-resolution via realistic downsampling with adversarial learning, *Phys. Med. Biol.* 66 (20) (2021) 205004.
- [30] H. Yu, S. Wang, Y. Fan, G. Wang, J. Li, C. Liu, Z. Li, J. Sun, Large-factor Micro-CT super-resolution of bone microstructure, *Front. Phys.* 10 (2022).
- [31] F. Maes, D. Loeckx, D. Vandermeulen, P. Suetens, Image registration using mutual information, in: N. Paragios, J. Duncan, N. Ayache (Eds.), *Handbook of Biomedical*

- Imaging: Methodologies and Clinical Research, Springer US, Boston, MA, 2015, pp. 295–308.
- [32] `tf.keras.losses.CategoricalCrossentropy`. https://www.tensorflow.org/api_docs/python/tf/keras/losses/CategoricalCrossentropy.
- [33] `tf.keras.optimizers.Adadelta`. https://www.tensorflow.org/api_docs/python/tf/keras/optimizers/Adadelta#args.
- [34] C. Ledig, L. Theis, F. Huszár, J. Caballero, A. Cunningham, A. Acosta, A. Aitken, A. Tejani, J. Totz, Z. Wang, W. Shi, Photo-realistic single image super-resolution using a generative adversarial network, in: 2017 IEEE Conference on Computer Vision and Pattern Recognition (CVPR), 2017, pp. 105–114.
- [35] I. Goodfellow, J. Pouget-Abadie, M. Mirza, B. Xu, D. Warde-Farley, S. Ozair, A. Courville, Y. Bengio, Generative adversarial nets, in: Advances in Neural Information Processing Systems, 2014, p. 27.
- [36] K. He, X. Zhang, S. Ren, J. Sun, Deep residual learning for image recognition, Proc. IEEE Conf. Comput. Vis. Pattern Recognit. (2016) 770–778.
- [37] J. Johnson, A. Alahi, L. Fei-Fei, Perceptual Losses for Real-Time Style Transfer and Super-Resolution, Springer International Publishing, Cham, 2016, pp. 694–711.
- [38] J. Bruna, P. Sprechmann, Y. LeCun, "Super-resolution with deep convolutional sufficient statistics," arXiv preprint. arXiv:1511.05666, 2015.
- [39] A. Dosovitskiy, T. Brox, Generating images with perceptual similarity metrics based on deep networks, Adv. Neural Inf. Proces. Syst. 29 (2016).
- [40] H.A. Aly, E. Dubois, Image up-sampling using total-variation regularization with a new observation model, IEEE Trans. Image Process. 14 (10) (2005) 1647–1659.
- [41] W. Zhou, A.C. Bovik, H.R. Sheikh, E.P. Simoncelli, Image quality assessment: from error visibility to structural similarity, IEEE Trans. Image Process. 13 (4) (2004) 600–612.
- [42] M. Spann, A. Nieminen, Adaptive Gaussian weighted filtering for image segmentation, Pattern Recogn. Lett. 8 (4) (1988) 251–255.
- [43] D.E.W. Whittier, The Assessment of Fragility Fracture Risk Using HR-pQCT as a Novel Tool for Diagnosis of Osteoporosis, 2021.
- [44] S. Hansen, V. Shanbhogue, L. Folkestad, M.M. Nielsen, K. Brixen, Bone microarchitecture and estimated strength in 499 adult Danish women and men: a cross-sectional, population-based high-resolution peripheral quantitative computed tomographic study on peak bone structure, Calcif. Tissue Int. 94 (3) (2014) 269–281.
- [45] L.A. Burt, H.M. Macdonald, D.A. Hanley, S.K. Boyd, Bone microarchitecture and strength of the radius and tibia in a reference population of young adults: an HR-pQCT study, Arch. Osteoporos 9 (2014) 183.
- [46] E. Sornay-Rendu, S. Boutroy, F. Duboeuf, R.D. Chapurlat, Bone microarchitecture assessed by HR-pQCT as predictor of fracture risk in postmenopausal women: the OFELY study, J. Bone Miner. Res. 32 (6) (2017) 1243–1251.
- [47] J.P. van den Bergh, P. Szulc, A.M. Cheung, M. Bouxsein, K. Engelke, R. Chapurlat, The clinical application of high-resolution peripheral computed tomography (HR-pQCT) in adults: state of the art and future directions, Osteoporos. Int. 32 (8) (2021) 1465–1485.
- [48] N. Mikolajewicz, N. Bishop, A.J. Burghardt, L. Folkestad, A. Hall, K.M. Kozloff, P. T. Lukey, M. Molloy-Bland, S.N. Morin, A.C. Offiah, J. Shapiro, B. van Rietbergen, K. Wager, B.M. Willie, S.V. Komarova, F.H. Glorieux, HR-pQCT measures of bone microarchitecture predict fracture: systematic review and Meta-analysis, J. Bone Miner. Res. 35 (3) (2020) 446–459.
- [49] P.K. Zysset, R.W. Goulet, S.J. Hollister, A global relationship between trabecular bone morphology and homogenized elastic properties, J. Biomech. Eng. 120 (5) (1998) 640–646.
- [50] E.J. Samelson, K.E. Broe, H. Xu, L. Yang, S. Boyd, E. Biver, P. Szulc, J. Adachi, S. Amin, E. Atkinson, C. Berger, L. Burt, R. Chapurlat, T. Chevalley, S. Ferrari, D. Goltzman, D.A. Hanley, M.T. Hannan, S. Khosla, C.-T. Liu, M. Lorentzon, D. Mellstrom, B. Merle, M. Nethander, R. Rizzoli, E. Sornay-Rendu, B. Van Rietbergen, D. Sundh, A.K.O. Wong, C. Ohlsson, S. Demissie, D.P. Kiel, M. L. Bouxsein, Cortical and trabecular bone microarchitecture as an independent predictor of incident fracture risk in older women and men in the Bone Microarchitecture International Consortium (BoMIC): a prospective study, Lancet Diab. Endocrinol. 7 (1) (2019) 34–43.
- [51] M. Yanagawa, A. Hata, O. Honda, N. Kikuchi, T. Miyata, A. Uranishi, S. Tsukagoshi, N. Tomiyama, Subjective and objective comparisons of image quality between ultra-high-resolution CT and conventional area detector CT in phantoms and cadaveric human lungs, Eur. Radiol. 28 (12) (2018) 5060–5068.
- [52] R. Kakinuma, N. Moriyama, Y. Muramatsu, S. Gomi, M. Suzuki, H. Nagasawa, M. Kusumoto, T. Aso, Y. Muramatsu, T. Tsuchida, K. Tsuta, A.M. Maeshima, N. Tochigi, S. Watanabe, N. Sugihara, S. Tsukagoshi, Y. Saito, M. Kazama, K. Ashizawa, K. Awai, O. Honda, H. Ishikawa, N. Koizumi, D. Komoto, H. Moriya, S. Oda, Y. Oshiro, M. Yanagawa, N. Tomiyama, H. Asamura, Ultra-high-resolution computed tomography of the lung: image quality of a prototype scanner, PLoS One 10 (9) (2015) e0137165.
- [53] L.J. Oostveen, K.L. Boedeker, M. Brink, M. Prokop, F. de Lange, I. Sechopoulos, Physical evaluation of an ultra-high-resolution CT scanner, Eur. Radiol. 30 (5) (2020) 2552–2560.
- [54] A.M. Hernandez, P. Wu, M. Mahesh, J.H. Siewerdsen, J.M. Boone, Location and direction dependence in the 3D MTF for a high-resolution CT system, Med. Phys. 48 (6) (2021) 2760–2771.
- [55] G. Shi, S. Subramanian, Q. Cao, S. Demehri, J. Siewerdsen, W. Zbijewski, Application of a Novel Ultra-high Resolution Multi-Detector CT in Quantitative Imaging of Trabecular Microstructure, SPIE, 2020.
- [56] F.I. Baffour, K.N. Glazebrook, A. Ferrero, S. Leng, C.H. McCollough, J.G. Fletcher, K. Rajendran, Photon-counting detector CT for musculoskeletal imaging: a clinical perspective, AJR Am. J. Roentgenol. 220 (4) (2023) 551–560.
- [57] F.S.L. Thomsen, S. Horstmeier, J.H. Niehoff, J.A. Peña, J. Borggrefe, Effective spatial resolution of photon counting CT for imaging of trabecular structures is superior to conventional clinical CT and similar to high resolution peripheral CT, Invest. Radiol. 57 (9) (2022) 620–626.
- [58] J.A. Peña, L. Klein, J. Maier, T. Damm, H.-P. Schlemmer, K. Engelke, C.-C. Glüer, M. Kachelrieß, S. Sawall, Dose-efficient assessment of trabecular microstructure using ultra-high-resolution photon-counting CT, Z. Med. Phys. 32 (4) (2022) 403–416.
- [59] F. Azari, P. Uniyal, J. Soete, W. Coudyzer, C.E. Wyers, J. Quintiens, J.P. van den Bergh, G.H. van Lenthe, Accuracy of photon-counting computed tomography for the measurement of bone quality in the knee, Bone 181 (2024) 117027.